# PI-line difference for alignment and motion-correction of cone-beam helical-trajectory micro-tomography data

Olaf Delgado-Friedrichs[1,2,*] Andrew M. Kingston[1,2,*], Shane J. Latham[1,2], Glenn R. Myers[1,2], and Adrian P. Sheppard[1,2]

***Abstract*—In micro-tomography, variants of helical X-ray source trajectories, e.g., double-helix (DH) and space-filling (SF), are attractive alternatives to the conventional circular trajectory, as they satisfy data-sufficiency conditions; this enables exact reconstruction, and large cone-angle (or high flux) imaging. Geometric alignment of micro-tomography experimental data, i.e., radiographs or projection data, to the required micron precision is a difficult problem. Here we consider criteria based on differences in attenuation along opposing rays as a post-acquisition software alignment technique. These opposing rays are called PI-lines and lie on lines that intersect two points of the scanning trajectory and pass through the region of support. The PI-line difference method is particularly appealing due to its low computational cost and small set of inherent assumptions, however, previous studies have exposed some limitations in precision. The number and distribution of PI-lines is highly dependent on the trajectory and thus so is the robustness of PI-line difference; here we show that DH and SF trajectories are particularly amenable to this technique. For these trajectories, we observe that the technique is applicable to both static and per-projection alignment estimation. We present results where PI-line difference alignment estimates are of equivalent accuracy as alignment estimates obtained from existing state-of-the-art methods: a tomogram sharpness method for static alignment and a re-projection-alignment method for per-projection alignment. In both cases, the computational expense of PI-line difference alignment estimation is a fraction of the tomogram-based methods.**

## I. Introduction

COMPUTED tomography (CT) generates non-destructive volumetric images of specimens in order to understand and quantify the internal structure and composition, enabling modeling of mechanical and transport properties. Many applications require high-resolution, high-fidelity CT microscopy (micro-CT) and even ultra-microscopy; for example: measuring porosity and pore-size distribution down to the sub-micron scale in oil-bearing rocks [1]; or identifying precise grain contacts in a granular material to create a force network to model mechanical compression and visualise stress and strain [2].

[1] Dept. of Applied Mathematics, Research School of Physics and Engineering, The Australian National University, Canberra, ACT 2601, Australia.
[2] CTLab: National Laboratory for Micro Computed-Tomography, Advanced Imaging Precinct, The Australian National University, Canberra, ACT 2601, Australia.
∗ Corresponding authors, email: Olaf.Delgado-Friedrichs@anu.edu.au, andrew.kingston@anu.edu.au
Manuscript received Month Day, 2017; revised Month Day, 2017.

CTLab, at the Australian National University, achieves high flux (and therefore high signal-to-noise ratio [SNR]) imaging with lab-based micro-focus X-ray sources by employing variants of helical trajectories [3], [4], [5]. Helical trajectories satisfy data sufficiency conditions [6] allowing theoretically exact reconstruction [7], and enable imaging with extremely large X-ray cone-angles to maximise detected X-ray flux. Similar to low-pitch helices, the double-helix (DH) trajectory provides more uniform resolution [4]. The recently developed space-filling (SF) trajectory is optimised for iterative reconstruction enabling more physics to be incorporated and accounted for in order to produce a more physically meaningful and quantitative tomogram [8]. The DH and SF trajectories enable high SNR imaging, however, applications also require precise morphological information about shape and structure. In micron and sub-micron resolution lab-based CT, this information can be severely compromised by poor geometric alignment of the instrument components (namely the X-ray source, sample manipulator, and detector) and/or by the relative motion of these components or the specimen during data acquisition (e.g., due to thermal effects). Hardware alignment to the required accuracy is extremely challenging and can be achieved by imaging *calibration phantoms* specifically designed to simplify identification of misalignment [9], [10], [11], [12]. However, physical alignment can be a very time consuming procedure, particularly if the instrument has many degrees of freedom. Even if such alignment were achieved (or misalignment estimated through a phantom pre-scan), the motion of the specimen or system components during data acquisition can cause the instrument to *drift* out of alignment. This problem is often overcome in electron tomography with the use of *fiducial markers* attached to the specimen. These markers are identified in the projection images and tracked throughout the acquisition process to determine both global misalignment and the *dynamic* motion effects [13], [14], [15]. These surface markers can't be used for region-of-interest (ROI) tomography where the surface lies outside the field of view, and they are unsuitable for lab-based polychromatic X-ray imaging since the highly-attenuating markers cause beam-hardening artifacts. Therefore, to correct dynamic motion errors, post-acquisition determination of misalignment by software is preferable.

Software methods for reference-less post-acquisition alignment of projection data have been applied successfully for many years, in most cases eliminating the need for precise geometric alignment of instrument components. For example,

software alignment can be achieved in tomogram space by searching for alignment parameter values that optimise some fitness function such as: minimising specimen support [16], minimising artefacts outside specimen support [17], minimising entropy [18], or maximising sharpness [19]. Tomogram-based methods are compuationally costly, an O($N^3$) voxel tomogram requires O($N$) measured projection images of O($N^2$) pixels and tomographic reconstruction is performed in O($N^4$) operations. While the computational cost can be amelioriated through multi-resolution methods it invariably adds a significant overhead to the overall reconstruction time.

Faster alternative methods exist, in projection space, which have O($N^3$) complexity, e.g., tracking the center-of-mass (if the entire object is in the field-of-view) or minimising the difference in transmission/attenuation of the specimen along lines from opposing directions [20], [21], [22] or planes from various directions (epipolar consistency [23]). Lines that intersect the trajectory and pass through the region of specimen support are known as PI-lines [24]. Of course, the number and distribution of PI-lines (and thus the misalignment accuracy achievable using PI-line difference) is heavily dependent on the scanning trajectory. Panetta et al. [20] demonstrated that PI-line difference, given a circular scan, can be used to estimate detector offset and in-plane detector rotation. Kingston et al. [21] showed, for helical scanning, all alignment parameters can be estimated to within one *optimal unit* of accuracy. In a helical trajectory, each point in the tomogram lies on a unique PI-line [24], [25], thus PI-line difference is potentially more *accurate* than tomogram methods (where typically only tomogram subsets are reconstructed due to computational complexity). However, since the PI-line method uses integrated data (along lines or ray paths through the object/tomogram), PI-line difference was found to be less *precise* in [21].

Here, we illustrate the use of PI-line difference minimisation to estimate both static and time-varying mis-alignment parameters for the double-helix [4] and space-filling [8] trajectories. The positions of PI-line measurement pairs within projection images, for these variants of the helical trajectory, are particularly well dispersed which is the key point for reliable application of the method.

Artifacts can arise in tomography due to different types of motion: i) motion that can be modeled (e.g., repeatable or predictable motion), and ii) unpredictable or "random" motion. The first category can be accounted for by characterising the motion and correcting its effects (such as described by Sasov et al [26] for correcting source motion as it reaches thermal equilibrium). The second category of motion is far more challenging, particularly in the absence of pre-placed fiducial markers. Here, we will assume motion of instrument components or the specimen are possible, but that the specimen itself remains rigid (i.e., is not distorted or deformed) during scanning. In this case, motion can be compensated for exactly by specifying the correct geometry per-projection image. It is often sufficient to approximate the effect of a subset of the motion parameters by remapping the projection image to be closer to the assumed geometry. For example, center-of-mass can again be used here to correct for translation errors. This method is fast since it works on projection images directly. It is, however, restricted to cases where the entire specimen is in the field-of-view (FOV) at all times - rendering it unsuitable for all forms of helical scanning and can be compromised by even a slightly off-axis sample mount. The centre-of-mass method is also not robust to beam-hardening artifacts. Epipolar consistency can be used on a per-projection basis [27], and although this is applicable for long objects, it is limited by FOV constraints in region-of-interest (ROI) scanning. A more general solution exists that uses re-projection alignment or projection matching [28], [29], [30], [31] (and variations thereof e.g., [32], [33]). This technique is effective and not limited by FOV, however, it is a computationally expensive iterative method that requires tomographic reconstruction and re-projection at every step.

In what follows, we first define the geometry of a fine-focus cone-beam CT instrument in Sect. II. In Sect. III we describe the double-helix and space-filling trajectories compared with conventional circular and helical trajectories. PI-lines are defined in Sect. IV and in Sect. V we describe how they can be used for alignment by minimising ray-difference. In Sect. VI we validate global (static/geometric) alignment by ray-difference with both simulated data, by comparison to a known misalignment, and with experimental data by comparison with results from a sharpness-metric method [19]. The extension of the technique to identify and correct for time-varying motion is presented in Sect. VII; again using simulated data to demonstrate the technique and experimental data to validate the method against results from re-projection alignment [34]. The paper then makes some concluding remarks following a brief discussion.

## II. Cone-beam micro-tomography system geometry

Here we consider a lens-less fine-focus geometry where magnification is achieved through the expanding spherical wave-front of X-rays emitted from a micro- or nano-focus X-ray source ($S$) that is a distance $S_l$ from the rotation axis. A flat-panel detector ($D$) is located a distance $D_l$ from the rotation axis (in the opposite direction). The relative orientation of the system co-ordinates $(w, h, l)$ with respect to the specimen co-ordinates $(x, y, z)$ is specified by an elevation $z$ and a horizontal angle $\theta$, as depticted in Fig. 1.

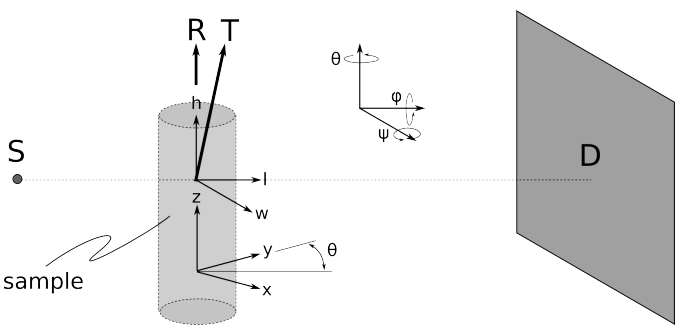


Fig. 1. A depiction of the system geometry with co-ordinates $(w, h, l)$ including the source ($S$), rotation axis ($R$), translation axis ($T$), and detector ($D$). The three rotations, $(\psi, \theta, \phi)$ ,and sample co-ordinates, $(x, y, z)$, are also shown.

There are 11 alignment parameters in total, defined here relative to the rotation-axis; three to describe the position of the detector, $(D_w, D_h, D_l)$, three to describe the orientation of the detector, $(D_\psi, D_\theta, D_\phi)$, another three to describe the source position, $(S_w, S_h, S_l)$, and two to describe the orientation of the sample manipulator translation axis, $(T_\psi, T_\phi)$. These have been depicted in Fig. 1.

In what follows, we have used a reduced seven-parameter model to define alignment (as proposed in [19]), so that results can be more easily compared with existing implementations of alignment [19], [3], [21]. This reduced set assumes the translation-axis is aligned with the rotation-axis, i.e., $T_\psi = T_\phi = 0$, and that in practice small lateral deviations of the source position are nearly indistinguishable from the analogous detector deviations, e.g., $D_w \approx -S_w S_l / D_l$. Alignment is then parameterised by the vector

$$\mathbf{p} = (D_w, D_h, D_l, D_\psi, D_\theta, D_\phi, S_l). \tag{1}$$

There is no reason to believe that the ray-difference method would be unable to treat the full parameter set, however there is little value for current hardware configurations.

## III. Cone-beam micro-tomography source/detector trajectories

Tomography requires input data of projection images (or radiographs) acquired from many different orientations about the sample. We define the path taken by the X-ray source about the sample as the *trajectory*. A conventional trajectory is circular (see Fig. 2a). This trajectory can be described as a height, $z$, along with a sequence of angles $\theta_i = i \cdot \Delta\theta$ for $i \in \mathbb{Z}_\Omega$ with $\Omega$ the total number of measured radiographs (or X-ray source positions) and $\Delta\theta$ giving the angular translation.

For 3D volumetric imaging, the circular trajectory does not satisfy data sufficiency conditions [6] and an approximate tomographic reconstruction results. A simple modification that can produce a trajectory sufficient for *exact reconstruction* is a vertical translation of $\Delta z$ between each source point. This results in a single-helix (SH) trajectory, (as depicted in Fig. 2b), which in this setting becomes a sequence of pairs $(z_i, \theta_i) = (i \cdot \Delta z, i \cdot \Delta\theta)$.

A double-helix trajectory typically uses fewer source points (or radiographs) per revolution than a helix, but incorporates an additional set of helical data with all angles, $\theta$, offset by $\pi$ (see Fig. 2c). For details on the definition, properties and advantages of the DH trajectory, we refer to [4]. It may be simpler to consider a very similar trajectory produced as a strided helix as follows: $(z_i, \theta_i) = (i \cdot \Delta z, i[\pi + \Delta\theta])$ for $i \in \mathbb{Z}_\Omega$.

A space-filling trajectory can be defined simply as a low-pitch helix with a large angular stride (scaled by $\alpha$ in the following), in which the corresponding pairs $(z_i, \theta_i) = (i \cdot \Delta z, i\alpha \cdot \Delta\theta)$ source points form an approximately hexagonal pattern (see Fig. 2d) in the $(z, \theta)$ plane. For details on the definition, properties and advantages of the SF trajectory, we refer to [8].

We note here that the SH, DH and SF trajectories all use an almost identical number of projections (source positions). Also, DH and SF trajectories are highly efficient in terms of dose and particularly efficient in a flux-limited micro-CT context because they allow *high cone angles*.

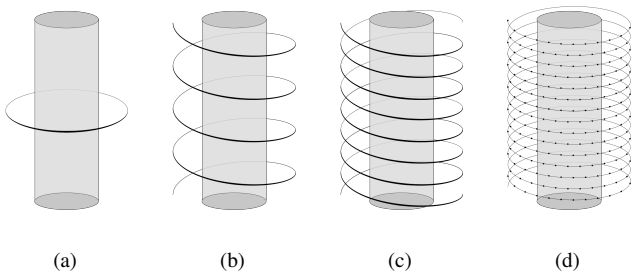

(a) (b) (c) (d)

Fig. 2. Schematic illustration of (a) circular, (b) helical, (c) double-helical and (d) space-filling trajectories. In the latter, the line represents the source motion profile and the points are positions of radiograph capture.

## IV. Explication of PI-lines

A PI-line is simply a line between two source positions which intersects the detector located at the corresponding source positions. Thus, there are a pair of detector measurements for X-rays attenuated along the same path (traversing the path in opposite directions) and ideally the two measurements should be consistent (equal). It is this pairwise consistency which we use as a measure of alignment. When the physical system geometry departs from the assumed geometry there will be inconsistency between the PI-line measurement pairs. We define PI-lines and associated measurement pairs more formally in the remainder of this section.

The center position of the source and detector at the $i^{\text{th}}$ radiographic measurement are found as $s_i = (-S_l \cdot \cos\theta_i, -S_l \cdot \sin\theta_i, z_i)$ and $d_i = (D_l \cdot \cos\theta_i, D_l \cdot \sin\theta_i, z_i)$, respectively. It is straightforward to compute the straight line (PI-line) between $s_i$ and $s_j$ for any index pair $i, j$, and thus obtain the detector value $r_{i,j}$ (if it exists) corresponding to the ray from $s_i$ going through $s_j$ in the $i^{\text{th}}$ radiograph. Pairs of source/detector positions that are too close in $\theta$ or too far in $z$ lead to PI-lines that do not intersect the detector, in which case the associated value $r_{i,j}$ will be undefined.

Fig. 3 shows example distributions PI-line detector positions corresponding to each of the trajectories depicted in Fig. 2. For a fixed source position $s_i$ and the corresponding fixed detector position, the Fig. 3 points are the source positions $s_j$ ($j = 1, \ldots, \Omega$) projected (from $s_i$) to the detector. These are the relevant detector positions used in the ray-difference computation that quantifies alignment, as described in the following section. Note that in Fig. 3, the number of points is approximately equal in each of 3(b), 3(c) and 3(d).

## V. Description of ray-difference

We define two matrices, $M = (m_{i,j})$ and $A = (a_{i,j})$ for $i, j \in \mathbb{Z}_\Omega$. Set $m_{i,j} = 1$ if both $r_{i,j}$ and $r_{j,i}$ are defined, $m_{i,j} = 0$ otherwise. Elements of $A$ are then found as $a_{i,j} = m_{i,j} \cdot r_{i,j}$. The accumulated ray difference along PI-lines is then computed as $e = \sum_{i,j}(a_{i,j} - a_{j,i})^2 / \sum_{i,j} m_{i,j}$. Repeating the computation based on a hypothetical misalignment of the system $S - D$, we derive an analogous value

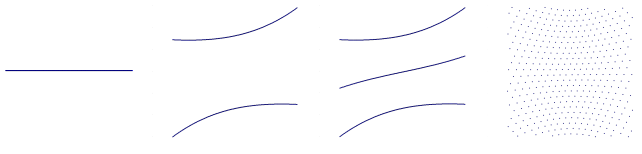

(a) (b) (c) (d)

Fig. 3. The distribution of PI-lines for the (a) circular (b) helical, (c) double-helical, (d) space-filling (or low-pitch large stride helical) trajectories as seen from a single fixed system position. For the circular trajectory PI-lines only exist in the sample mid-plane, meaning they provide more limited information; they are more uniformly dispersed for the double-helical and space-filling trajectories.

$e(\mathbf{p})$ for $\mathbf{p} \in \mathbf{P}$ the parameter vector describing misalignment (1). Note that any alignment variation can change which PI-lines hit or miss the detector, thus the normalization via the matrix $M$ is crucial. Our task is to find a vector $\mathbf{p}_{\min} \in \mathbf{P}$ that minimizes $e$; it is assumed that $\mathbf{p}_{\min}$ best describes the current system geometry. More generally, this method can, at least in principle, be applied to the post-acquisition estimation of any form of deviation from the idealized experiment that would result in a non-zero ray difference value $e$, such as irregularities in source flux, detector response, or changes to the sample itself.

The time complexity of computing $e(\mathbf{p})$ for a given parameter $\mathbf{p}$ is clearly $O(\Omega^2)$. The evaluation of each $r_{i,j}$ consists of a straightforward geometric computation followed by interpolating (sampling) a single value from the appropriate projection image, both of which are constant-time operations. The values $m_{i,j}$ and $a_{i,j}$ for given $i, j$ depend only on $r_{i,j}$ and $r_{j,i}$. Finally, the evaluation of the matrix norms requires summing the elements of two $\Omega \times \Omega$ matrices.

We note in particular that (ignoring memory access times) the execution time for ray-differencing does not depend on the resolution of the radiographs, but only on the number of projections taken into account. Tomogram sharpness methods, by contrast, require a filtered back-projection with time-complexity $O(\Omega \cdot N^3)$ for each evaluation, making its execution times highly sensitive to resolution and significantly more computationally demanding than ray-differencing in all practical scenarios.

Like any marker-free post-acquisition scheme, such as sharpness metrics [19] and epipolar consistency [23], the success of ray-difference minimisation depends on the specimen having sufficient contrast at appropriate length scales. A sample with insufficient structure, or insufficient variation in one direction, cannot be accurately aligned in that direction. Aside from this essential limitation, the ray difference method works directly with experimental projection data and does not require any further assumptions. It is also fully tolerant of X-ray beam hardening since the degree of beam hardening is equal for both traversals of the PI-line.

## VI. Ray-difference minimisation for correcting global (or static) misalignment

The parameter space defining a per-projection geometry has $7\Omega$ dimensions. This is far too large to search exhaustively. It is customary and convenient to first estimate a global (or static) alignment vector to account for unavoidable inaccuracies in the calibration of the instrument, i.e., assigning a single value to each parameter across all projections, in effect averaging out any time-dependent variations (or motion). Per-projection deviations from this global alignment due to thermal motion, sample manipulator inaccuracies, and other physical effects can be dealt with in a subsequent step.

### A. Simulating global misalignment

A collection of simulated global misalignment datasets were computed from a digital phantom of size $512 \times 512 \times 1024$ voxels (with a voxel size of $3.2\mu$m) by forward projecting with a number of prescribed misalignment vectors. A cross section of the phantom is shown in Fig. 4. The geometry was such that $S_l = 1.6384$mm and $D_l = 80.2816$mm, corresponding to a magnification factor of 50 and a detector pixel size of 0.16mm. The simulated detector size was 592 pixels along each axis, resulting in a cone angle of 60 degrees.

Each simulated experiment consisted of $\Omega = 1950$ radiographs taken along a total vertical extent of 5.4012mm, with a vertical increment of $\Delta z = 2.771\mu m$ and a radial increment of $\alpha\Delta\theta = 6.36^\circ$ between successive radiographs. The result from a single iteration of the multi-grid reconstruction [35] assuming a perfectly aligned projection set is shown in Fig. 4.

### B. Alignment procedure

In the results presented below, we estimate global alignment using the accumulated ray-difference as its cost function. We define the alignment parameter values that minimise this cost function as those that most accurately describe the instrument geometry.

The sensitivity of parameters varies: some can be optimised regardless of the value of the remaining parameters, while others require all parameters to be close to optimal first [19]. A sequence of 1D scans of each parameter in order from least sensitive to most sensitive (as described below) is a fast and effective technique to approach the correct instrument geometry. We have practically observed that the 7D cost function is smooth and well behaved in the vicinity of the correct instrument geometry. Local descent-based optimisation methods, such as the Powell method [36], can be used to refine the solution.

As in the case of the sharpness-based alignment correction in Kingston *et al* [19], a multi-resolution approach improves the robustness of convergence for larger misalignments since it broadens the peaks shown in Figure 6. Alignment in the 7D parameter space is determined in a multiscale iterative fashion with three-pass sequence of 1D scans, i.e., varying only a single parameter; an appropriate parameter scan order was demonstrated in [19]. In the first pass, a linear scan was performed for each parameter in order with a fixed step size and a fixed maximum distance below and above the previous parameter value. The step size was chosen as one optimal unit (OU, as defined in [19]) for that parameter, with a maximum scan range of 20 OU. After each individual scan, a

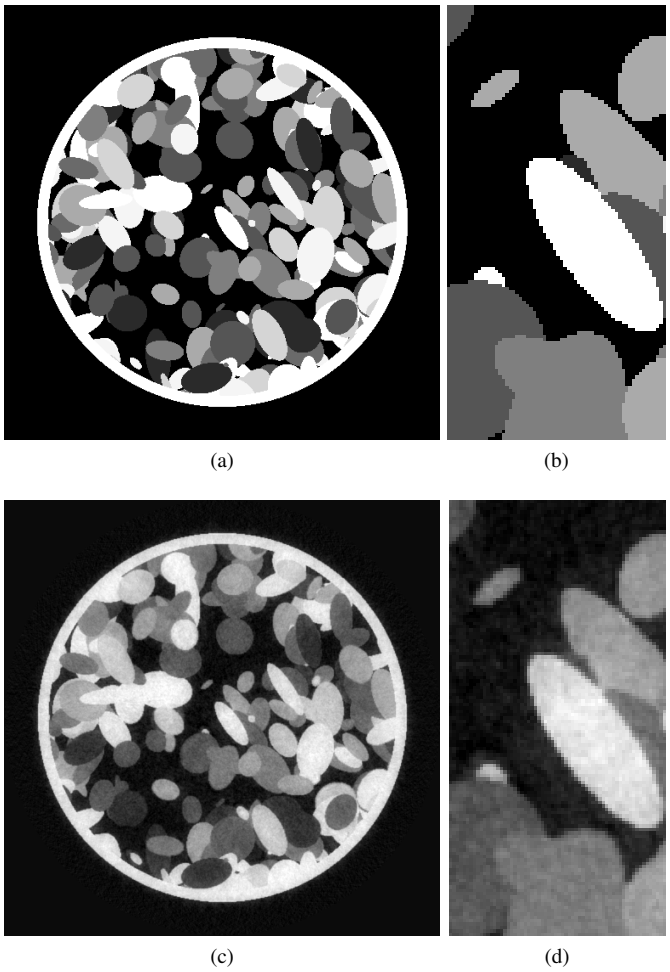

(a) (b) (c) (d)

Fig. 4. (a) A cross-section of the digital phantom used. (c) Single iteration of the multi-grid reconstruction from correctly aligned projections. (b,d) central region of (a,c) with 4x magnification.

new parameter value was calculated via a parabolic fit around the best measured value, and all subsequent scans proceeded using that new value. In the second pass, we applied Powell's method to identify a local optimum with the parameter vector determined by the first pass as a starting point. These first two passes were performed on a reduced dataset with each projection scaled down (binned) by a factor of 4 as well as a stride of 4, i.e. only taking every fourth projection into account. Finally in the third pass, we performed another series of linear scans, this time with a bin factor of 2, a stride of 1, and a scan range of 4 optimal units. These particular combinations of down-sampling and striding were chosen based on practical experience with sharpness-based alignment of real CT data at our facility.

### *C. Performance on simulated space-filling trajectory data with known misalignment*

Figure 5 shows the uncorrected and corrected reconstructions for a projection set taken with a SF trajectory and with simulated misalignments in all of the 7 parameters used in our simplified model. Here the magnitudes of the deviations resemble those we routinely experience in practice, in this case between approximately 3 and 15 optimal units, depending on the parameter. For the corrected reconstruction, we have applied an affine transformation to each projection based on the estimated parameters and reconstructed the result normally. Correction by detector transformation is an approximation only; for correcting larger errors it is more accurate to modify the trajectory itself, as discussed in section VIII.

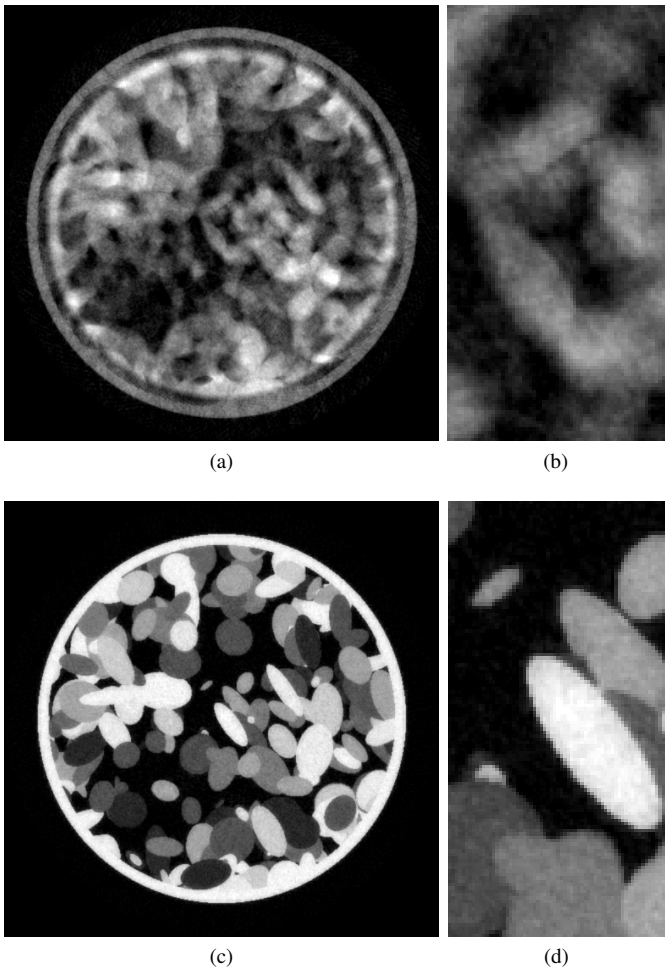

(a) (b) (c) (d)

Fig. 5. Reconstructions of a projection set taken with SF trajectory and simulated realistic misalignment in all 7 parameters. (a) uncorrected (c) ray difference alignment corrected. (b,d) 4x magnifications (from centers) of (a,c).

In Fig. 6 we illustrate the first and third (last) estimation phase as performed on this projection set. All parameters were correctly estimated within fractions of the respective optimal units. Some of the parameters, particularly $D_\theta$, are not estimated very well in the first pass, but the second pass is then able to compensate.

### *D. Validation on experimental double-helix trajectory data*

Figure 7 shows the uncorrected and corrected reconstructions for a cylindrical sample of white beech wood, 3mm in diameter, acquired with a double-helix trajectory using a total of 14136 projections (7068 per helix). The data was taken with $S_l = 3$mm and $D_l = 312.5$mm, $\Delta z = 1.344\mu$m and $\alpha\Delta\theta = 0.125°$. A $3040 \times 3040$ pixel detector with a pixel

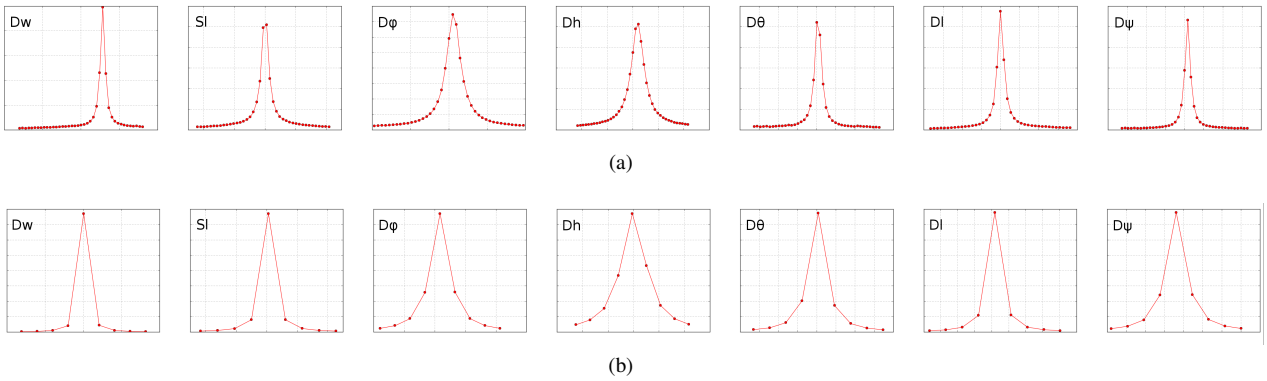


Fig. 6. Parameter scans for a projection set taken with SF trajectory and one example of simulated realistic misalignment in all 7 parameters: (a) initial coarse 1D scans of each parameter in sequence, (b) final refinement scans, again of each parameter in sequence. The $y$-axis is metric value (inverse of average squared ray-difference) and the $x$-axis is the respective parameter value. The dots mark individual evaluations of the quality function, spaced at intervals of one optimal unit.

size of 0.139mm was used. The effective cone angle was again $60^\circ$, and the magnification factor was 105.2.

In this case misalignments are not known. Instead we compare ray-differencing generated alignment correction parameters with those generated using minimization of a tomogram sharpness metric. Sharpness is calculated as the L2 norm of a representative sub-volume of the high-pass filtered tomogram. The tomogram is produced by ramp-filtered back-projection (FBP); ramp filtering is not technically the correct filter here, however, degradation of sharpness estimates are negligible since the resulting artifacts are low-frequency and edges are faithfully reconstructed. The seven alignment parameters are determined in a multiscale iterative fashion with a three-pass sequence of 1D scans. This particular strategy was chosen to give both methods an equal chance of convergence to a good estimate, while keeping the execution times for the sharpness method relatively low. Specifically, all evaluations were performed on down-sampled data, which significantly reduces time requirements for the sharpness metric calculations, but has no relevant efficiency implications for ray-differencing.

In Fig. 8 we illustrate the first estimation phase as performed on this projection set and compare with an equivalent sequence of parameter scans using a sharpness criterion. In both cases, we have used a binning factor of 4 and a stride of 4, with a maximum scan range of 20 OU. Following standard approaches, to reduce computational cost the sharpness calculations were performed on only the central set of ≈1000 out of a total of ≈3500 projections after striding. The ray difference calculations were performed on the full set. The execution time per evaluation was 5 seconds for sharpness and 0.1 seconds for ray difference.

The resulting estimates differed by slightly over 1 OU for $D_l$ and fractions of an OU for all other parameters. Thus all parameters are presumably within 1 OU of the actual geometry and are therefore equivalent (for the specified tomogram voxel size). A small difference in the result is not unexpected since the sharpness-alignment-parameters are calculated only over the central (≈1000) projections of the data set (as a computational saving) and the ray-difference-alignment parameters are calculated over the entire (≈3500 projection) data-set. The quality of the two tomograms, reconstructed from the sharpness and ray-difference parameter alignment corrections, was visually indistinguishable.

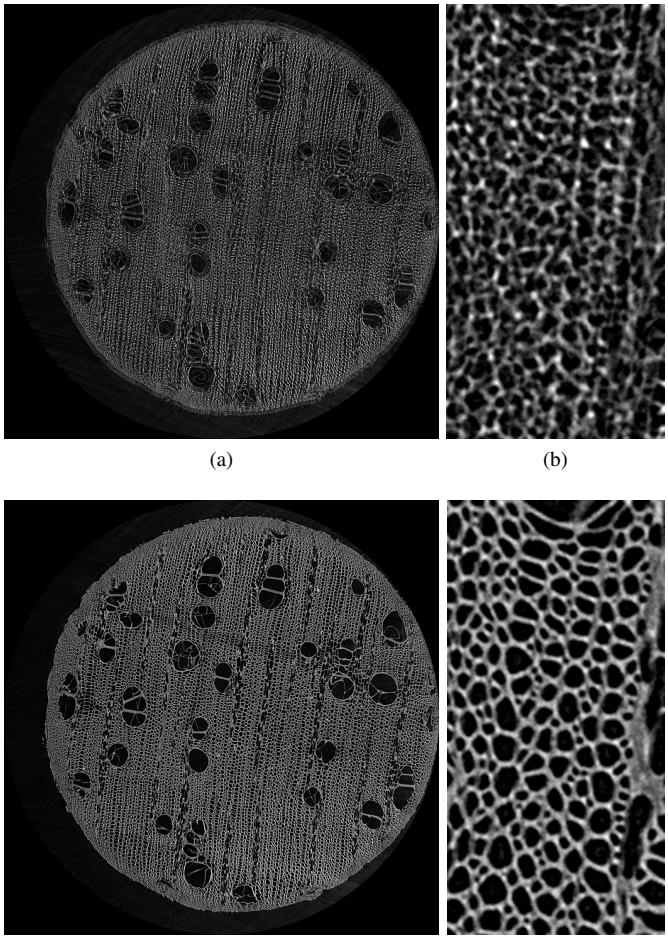


Fig. 7. Reconstruction of a white beech DH trajectory dataset. (a) uncorrected (c) ray difference. (b,e) 8x magnifications (from centers) of (a,c).

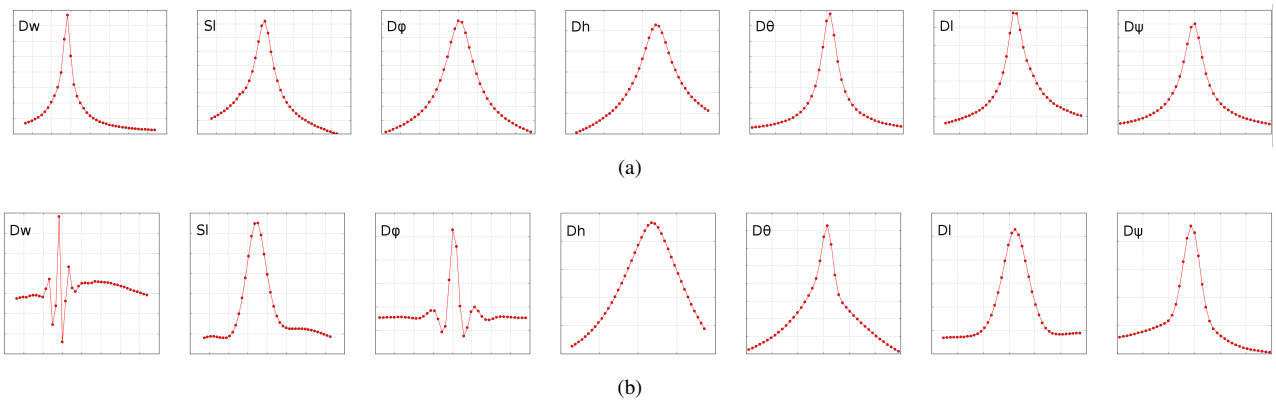


Fig. 8. Coarse-resolution parameter scans for white beech sample DH projection set: (a) inverse ray-difference and (b) sharpness. The $y$-axis is metric value and $x$-axis is the respective parameter value.

## VII. Ray-difference minimisation for correcting time-varying misalignment (or motion)

We demonstrate the ability of the ray-difference method to accurately detect per-projection deviations from an idealized trajectory using the simple iterative optimization process detailed below. In this case, deviations from an idealized trajectory will be caused by unplanned relative movement of the source, sample and/or detector, such as by inaccuracies in the sample stage or motion of the source or sample caused by thermal expansion. We have restricted our attention to a subset of the relevant geometry parameters, in this case the horizontal and vertical detector shift, in order to make our results more easily comparable with existing implementations, specifically the re-projection alignment method described in [34], [31].

A detector shift or rotation for the $i^{\text{th}}$ projection corresponds to a change in the $i^{\text{th}}$ row $(a_{i,j})_{j=1}^{\Omega}$ of the matrix $A$, but leaves the $i^{\text{th}}$ column unchanged, whereas a deviation in the position of the x-ray source would change both the row and column. In either case, in order to evaluate the corresponding change in the accumulated ray difference $e$, we only need to recompute the normalized differences between the $i^{\text{th}}$ row and $i^{\text{th}}$ column.

Our optimization scheme attempts to find the best detector shift for each projection in turn relative to all the others by a sequence of two linear scans, one horizontal and one vertical, with a fixed step-size of one pixel and a distance of 10 pixels. As in Sect. VI, a sub-pixel optimum was then estimated via a parabolic fit. As a dampening measure, the new shift estimate was taken mid-way between the old one and the new optimum. After all projections were processed in this way, the previous shift estimates were replaced with the new ones and a new iteration started. We ran 10 iterations in our experiments, using the complete set of radiographs at full resolution.

### A. Simulating time-varying misalignment

The same simulation phantom and setup were used as in Section VI-A to evaluate our ray-difference based motion estimation procedure. Here, a simulated projection set was computed with a pre-determined sequence of detector shifts based on appropriately re-sampled motion data from a real experiment. In our implementation, individual per-projection shifts were applied by manipulating the positions of the detector center when calculating the forward projection, rather than transforming the projection image after the fact.

### B. Performance on simulated double-helix trajectory data with known motion

Figure 9 shows a comparison of estimated and true shifts for the ray-differencing method. We can see that the estimation error remains well below a pixel (or 1 OU) except in the regions that correspond to the top and bottom ends of the helices, where there is insufficient data for a meaningful estimation. In our implementation, we have set the estimates to zero whenever fewer than 10 PI-lines were available for a given projection.

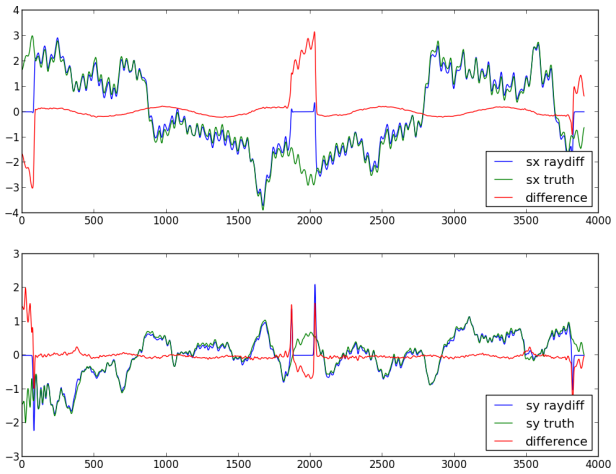


(a)

Fig. 9. Motion estimation versus ground truth using the inverse ray difference metric ($x$-axis is projection number and $y$-axis is pixel shift).

Figure 10 shows two reconstruction results for this projection set, one uncorrected and the other using motion correction via ray-differencing. One can observe that the double-edge artifacts due to motion errors have been removed by this motion correction process.

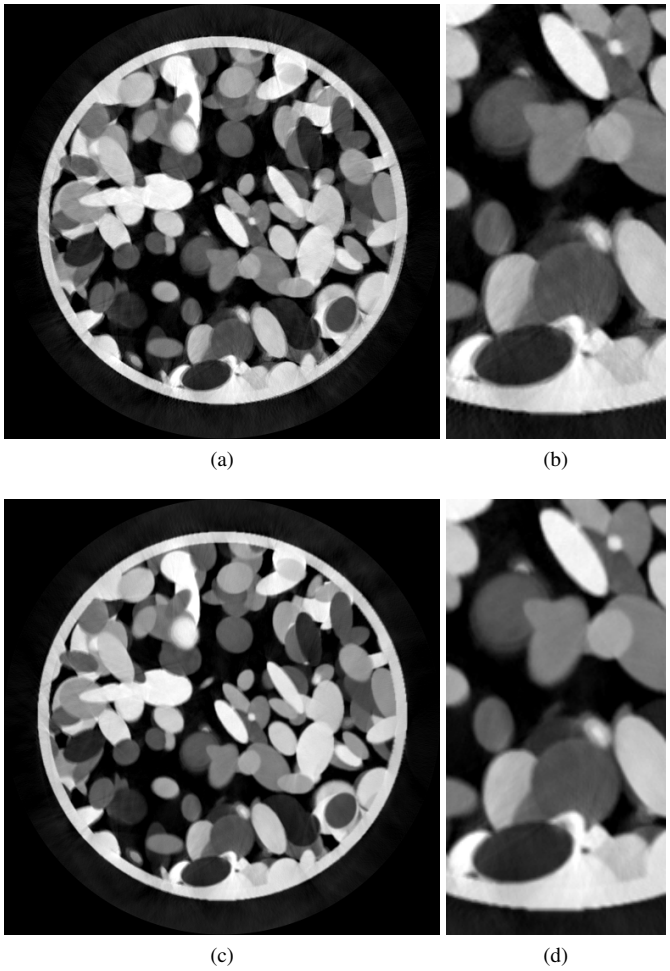

(a) (b) (c) (d)

Fig. 10. Reconstructions of a DH projection set with simulated detector motion. (a) uncorrected (c) motion correction via ray-difference. (b,d) 2x magnifications (from bottom centers) of (a,c).

### C. Validation on experimental space-filling trajectory data

Figure 11 shows two reconstructions of 5mm Edwards limestone core, one with only global alignment, the other with additional motion correction. The data was acquired with a space-filling trajectory using 4858 projections, at $S_l = 7.1$mm, $D_l = 335.6$mm, $\Delta z = 4.529\mu$m and $\alpha\Delta\theta = 3.285°$. A $2272 \times 2272$ pixel detector with a pixel size of 0.139mm was used. The effective cone angle was $45°$, and the magnification factor was 47.3. In the magnified detail pictures, one can see a subtle but important increase in detail and sharpness.

For this experimental data, the per-projection misalignments are not known a-priori. Instead, we compare PI-line difference optimization estimates with estimates produced by the multi-resolution re-projection alignment method [31]. The re-projection method generates *simulated* projections from a reconstructed tomogram and estimates per-projection motion parameters by image-registration of corresponding pairs of simulated and experiment projections. Multiple iterations are performed before obtaining the final per-projection motion estimates.

Figure 12 shows a comparison of the estimated shifts using the ray-difference method and the re-projection method. Both methods agree to within a fraction of a detector pixel (or 1 OU), which is particularly obvious for the horizontal shifts, but also true for the generally smaller vertical ones. We ran both methods on six computation cores. The re-projection method execution time was approximately an hour for a total of six iterations (four iterations at a quarter and two at half resolution), using a highly optimized GPU implementation for forward- and back-projection implementation, and ray-difference execution time was approximately ten minutes for 50 iterations (at full resolution), without optimisation. Please see section VIII for further discussion of these results.

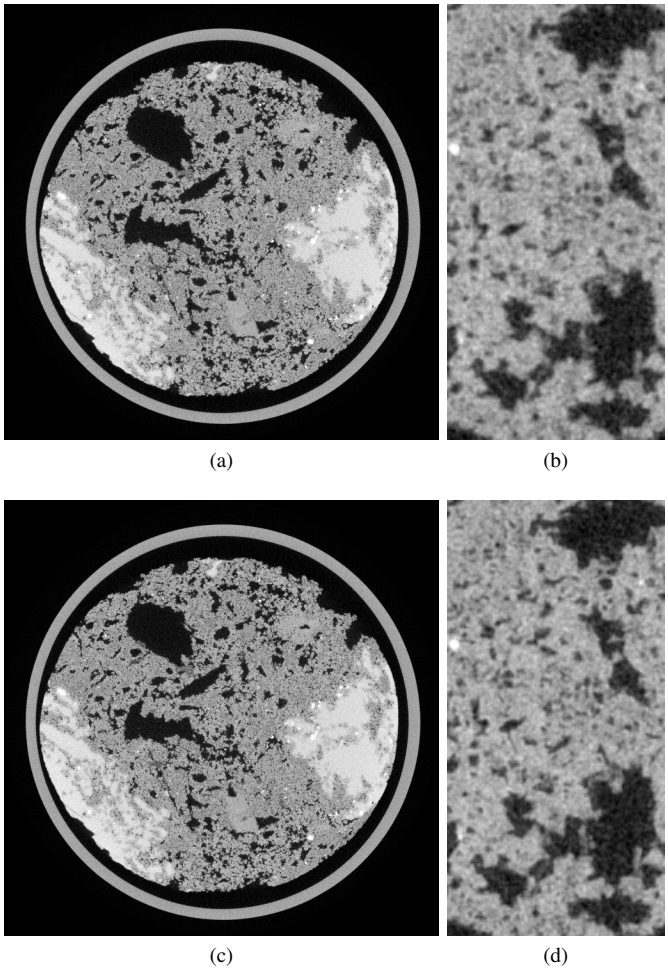

(a) (b) (c) (d)

Fig. 11. Reconstruction of a combined sandstone/limestone SF dataset (horizontal slice showing limestone) (a) without (c) with motion correction. (b,e) 8x magnifications (from centers) of (a,c).

## VIII. Discussion

The ray-difference metric relies on the idea that in a sufficiently small neighborhood of the true PI-line connecting two source positions, the difference between the corresponding (interpolated) projection values is also small and depends monotonically on the amount of displacement. This is not necessarily true in reality, due to noise, intensity fluctuations, low-detail regions in the projections and other factors. By taking a large number of source position pairs into account, however, these irregularities tend to average out, depending on

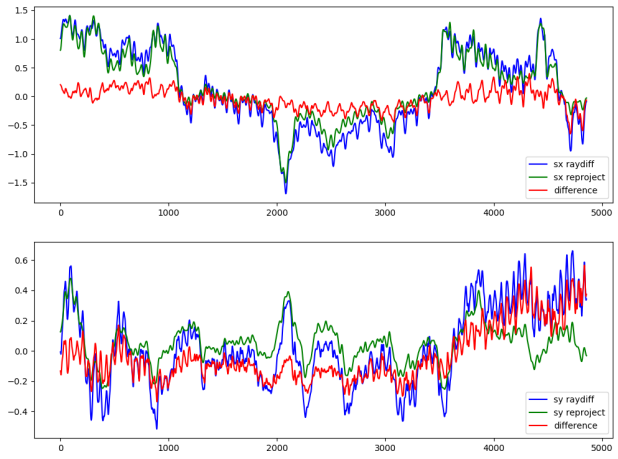


(a)

Fig. 12. Motion estimation in sandstone/limestone dataset using the inverse ray difference metric versus the re-projection method ($x$-axis is projection number, $y$-axis is pixel shift).

the nature of the data set and in particular the type of trajectory used. We would expect the most robust behavior from a trajectory in which projected source positions are evenly distributed over most of the detector surface, as is the case for the space-filling trajectory, and indeed our observations so far seem to validate this. We acknowledge that there are likely to be degenerate cases (objects) which potentially produce a flat cost function (ray-difference sum), particularly in some of the alignment parameter directions. However, these cases (such as low contrast and low-feature objects) are challenging for all a-posteriori alignment methods.

Work with experimental data has shown that the ray-difference metric is more sensitive to intensity fluctuations between projections than for example the sharpness metric, especially in the case of DH trajectory datasets. In the example shown in Fig. 7, global alignment using ray-difference originally failed due to insufficient intensity correction in the preprocessing stage. We were able to compensate for this by subtracting from each projection frame the mean ray-difference along all its PI-lines and repeating this procedure 20 times, after which the performance of the global alignment procedure was comparable to that for SF trajectory data (c.f. Figures 7 and 8). This compensation strategy worked well in this case due to the homogeneity of the sample along the z-axis, but is of course far too simplistic in general. It leads us to believe, however, that in principle one could apply ray-difference methods successfully to the problem of a-posteriori intensity correction, leading to higher quality images.

Note that we have corrected for misalignment and motion by affine transformation of projection images. This is a reasonable approximation for systems with a low cone-angle geometry and for small misalignments in high cone-angle systems. However, for large misalignments (or large motion) in high cone-angle systems the angles of ray paths through the specimen can change significantly. In this case correction by allowing the X-ray source to translate will provide a better approximation to these correct ray paths. A per-projection change in source position yields a change in geometry, which is more complicated to implement, and possibly a change in filtering (for FBP type reconstruction schemes). This is a topic for future work.

The global alignment examples shown demonstrate that the ray-difference metric works just as well with binned and strided data as does the tomogram sharpness metric. We expect similar results when correcting time-dependent misalignment, but have not yet verified this. Ray-difference based alignment methods could thus potentially be integrated within iterative multi-grid reconstruction schemes.

## IX. Conclusion

We have presented the concept of PI-lines and a method to quantify misalignment by defining the accumulated ray-difference between measured PI-line attenuation. We demonstrated that the misalignment of a CT instrument can be determined for both static and time-varying mis-alignments by minimising this metric (cost function). This PI-line difference metric is evaluated directly in projection space which is O($N$) times faster than methods which require $N^3$ voxel tomograms to be calculated such as the sharpness metric for global alignment, and the re-projection-alignment method for per-projection alignment. The PI-line difference method produced alignment estimates on real experimental data to within 1OU of the estimates produced by sharpness for static alignment and by re-projection for time-varying alignment. Additionally, the ray difference cost function was practically observed (Fig. 8) to have a larger radius of convergence and to be more amenable to local descent-based optimisation techniques (improved smoothness and convexity) when compared to sharpness for static alignment estimation. Full support of the specimen is not required for PI-line difference, thus region-of-interest data can be aligned using this technique.

Reliability/robustness of the PI-line difference method is directly related to spatial distribution of the projected source points (Fig. 3). The more uniform the spatial sampling across the detector the greater the likelihood of a well-behaved cost function (smooth, large global minimum capture radius). All helical trajectories, except very high-pitch single helices (namely Katsevich one-PI trajectories) should provide sufficiently dispersed PI-lines for the method to work effectively. To our knowledge, no reliable a-posteriori methods exist for high-pitch single-helices, since these trajectories don't provide opposing viewing angles and therefore mis-alignments manifest in the reconstruction as high-frequency artefacts, rather than as blur. While it is conceivable that there exist degenerate cases (objects) for which the PI-line difference optimisation fails to accurately estimate alignment parameters, it is also likely that PI-line difference optimisation is capable of accurately estimating alignment parameters in cases where methods such as sharpness-optimization and re-projection-alignment fail and therefore provides a computationally cheap and robust alternative to these tomogram-based methods.

## Acknowledgment

The authors acknowledge the financial support of the Australian Research Council and FEI-Thermo Fisher Scientific

through Linkage Project LP150101040, and the use of supercomputer time provided by Australia's National Computational Infrastructure (NCI). We thank Mohammad Saadatfar for providing the beech data set and Levi Beeching and Michael Turner from the ANU CTLab for data acquisition.

## REFERENCES


[1] R. M. Sok, M. A. Knackstedt, T. Varslot, A. Ghous, S. Latham, A. P. Sheppard *et al.*, "Pore scale characterization of carbonates at multiple scales: Integration of micro-ct, bsem, and fibsem," *Petrophysics*, vol. 51, no. 06, 2010.

[2] M. Saadatfar, A. P. Sheppard, T. J. Senden, and A. J. Kabla, "Mapping forces in a 3d elastic assembly of grains," *Journal of the Mechanics and Physics of Solids*, vol. 60, no. 1, pp. 55–66, 2012.

[3] T. Varslot, A. Kingston, G. Myers, and A. Sheppard, "High-resolution helical cone-beam micro-ct with theoretically-exact reconstruction from experimental data," *Medical physics*, vol. 38, no. 10, pp. 5459–5476, 2011.

[4] ——, "Considerations for high-magnification high-cone-angle helical micro-ct," *SPIE Optical Engineering+ Applications*, pp. 850 614–850 614, 2012.

[5] A. M. Kingston, G. R. Myers, S. J. Latham, J. P. Veldkamp, and A. P. Sheppard, "Optimized X-ray source scanning trajectories for iterative reconstruction in high cone-angle tomography," in *Optics and Photonics: Developments in X-Ray Tomography X*, ser. Proc. SPIE, S. R. Stock, Ed., vol. 9967, 2016, pp. 9967–38.

[6] T. H, "An inverse formula for cone-beam reconstruction," *SIAM Journal of Applied Math.*, vol. 43, pp. 546–552, 1983.

[7] A. Katsevich, "Theoretically exact filtered backprojection-type inversion algorithm for spiral CT," *SIAM Journal on Applied Mathematics*, vol. 62, no. 6, pp. 2012–2026, 2002. [Online]. Available: http://epubs.siam.org/doi/abs/10.1137/S0036139901387186

[8] A. M. Kingston, G. R. Myers, S. J. Latham, B. Recur, H. Li, and A. P. Sheppard, "Space-filling x-ray source trajectories for efficient scanning in large-angle cone-beam computed tomography," *IEEE Transactions on Computational Imaging*, 2018. [Online]. Available: https://doi.org/10.1109/TCI.2018.2841202

[9] A. V. Bronnikov, "Virtual alignment of x-ray cone-beam tomography system using two calibration aperture measurements," *Optical Engineering*, vol. 38, no. 2, pp. 381–387, 1999.

[10] Y. Sun, Y. Hou, F. Zhao, and J. Hu, "A calibration method for misaligned scanner geometry in cone-beam computed tomography," *Ndt & E International*, vol. 39, no. 6, pp. 499–513, 2006.

[11] K. Yang, A. L. Kwan, D. F. Miller, and J. M. Boone, "A geometric calibration method for cone beam ct systems," *Medical physics*, vol. 33, no. 6Part1, pp. 1695–1706, 2006.

[12] C. Mennessier, R. Clackdoyle, and F. Noo, "Direct determination of geometric alignment parameters for cone-beam scanners," *Physics in Medicine & Biology*, vol. 54, no. 6, p. 1633, 2009.

[13] J. C. Fung, W. Liu, W. J. De Ruijter, H. Chen, C. K. Abbey, J. W. Sedat, and D. A. Agard, "Toward fully automated high-resolution electron tomography," *Journal of structural biology*, vol. 116, no. 1, pp. 181–189, 1996.

[14] D. N. Mastronarde, "Fiducial Marker and Hybrid Alignment Methods for Single- and Double-axis Tomography," in *Electron Tomography*. Springer, New York, NY, 2007, pp. 163–185, dOI: 10.1007/978-0-387-69008-7_6.

[15] R. Han, F. Zhang, X. Wan, J.-J. Fernández, F. Sun, and Z. Liu, "A marker-free automatic alignment method based on scale-invariant features," *Journal of structural biology*, vol. 186, no. 1, pp. 167–180, 2014. [Online]. Available: https://doi.org/10.1016/j.jsb.2014.02.011

[16] A. Brunetti and F. De Carlo, "A robust procedure for determination of center of rotation in tomography," in *Developments in X-Ray Tomography IV*, vol. 5535. International Society for Optics and Photonics, 2004, pp. 652–660.

[17] A. Viskoe, "Computed tomography postacquisition data correction for system alignment errors," *IEEE Transactions on instrumentation and measurement*, vol. 48, no. 5, pp. 972–977, 1999.

[18] Y. Kyriakou, R. Lapp, L. Hillebrand, D. Ertel, and W. Kalender, "Simultaneous misalignment correction for approximate circular cone-beam computed tomography," *Physics in Medicine & Biology*, vol. 53, no. 22, p. 6267, 2008.

[19] A. Kingston, A. Sakellariou, T. Varslot, G. Myers, and A. Sheppard, "Reliable automatic alignment of tomographic projection data by passive auto-focus," *Medical physics*, vol. 38, no. 9, pp. 4934–4945, 2011.

[20] D. Panetta, N. Belcari, A. Del Guerra, and S. Moehrs, "An optimization-based method for geometrical calibration in cone-beam ct without dedicated phantoms," *Physics in Medicine & Biology*, vol. 53, no. 14, p. 3841, 2008.

[21] A. Kingston, T. Maniotis, T. Varslot, G. Myers, A. Shappard, J. Trumpf, and R. Hartley, "Geometric alignment of helical tomographic projection data using pi-lines," in *Proc. Int. Conf. on Tomography of Materials and Structures (ICTMS)*, vol. 9967, 2013, pp. 101–104.

[22] Delgado-Friedrichs, A. M. Kingston, S. J. Latham, G. R. Myers, and A. P. Sheppard, "Geometric alignment of cone-beam helical-trajectory micro-tomography data using a pi-line difference metric," in *Proc. of the Int. Conf. on X-Ray Microscopy 2018*. Microscopy and Microanalysis, 2018, p. To be determined...

[23] A. Aichert, M. Berger, J. Wang, N. Maass, A. Doerfler, J. Hornegger, and A. K. Maier, "Epipolar consistency in transmission imaging," *IEEE transactions on medical imaging*, vol. 34, no. 11, pp. 2205–2219, 2015.

[24] P.-E. Danielsson, P. Edholm, J. Eriksson, and M. M. Seger, "Towards exact reconstruction for helical cone-beam scanning of long objects. a new detector arrangement and a new completeness condition," in *Proc. 1997 Meeting on Fully 3D Image Reconstruction in Radiology and Nuclear Medicine (Pittsburgh)(DW Townsend and PE Kinahan, eds.)*, 1997, pp. 141–144.

[25] M. Defrise, F. Noo, and H. Kudo, "A solution to the long-object problem in helical cone-beam tomography," *Physics in Medicine & Biology*, vol. 45, no. 3, p. 623, 2000.

[26] A. Sasov, X. Liu, and P. L. Salmon, "Compensation of mechanical inaccuracies in micro-CT and nano-CT," in *Optics and Photonics: Developments in X-Ray Tomography VI*, ser. Proc. SPIE, S. R. Stock, Ed., vol. 7078, San Diego, California, USA, 2008, pp. 7078–1C. [Online]. Available: http://proceedings.spiedigitallibrary.org/proceeding.aspx?articleid=794895

[27] B. Bier, A. Aichert, L. Felsner, M. Unberath, M. Levenston, G. Gold, R. Fahrig, and A. Maier, "Epipolar consistency conditions for motion correction in weight-bearing imaging," in *Bildverarbeitung für die Medizin 2017*. Springer, 2017, pp. 209–214.

[28] J. Dengler, "A multi-resolution approach to the 3d reconstruction from an electron microscope tilt series solving the alignment problem without gold particles," *Ultramicroscopy*, vol. 30, no. 3, pp. 337–348, Jul. 1989.

[29] S. Mayo, P. Miller, D. Gao, and J. Sheffield-Parker, "Software image alignment for X-ray microtomography with submicrometre resolution using a SEM-based X-ray microscope," *Journal of microscopy*, vol. 228, no. 3, pp. 257–263, 2007. [Online]. Available: http://onlinelibrary.wiley.com/doi/10.1111/j.1365-2818.2007.01857.x/full

[30] D. Gürsoy, Y. P. Hong, K. He, K. Hujsak, S. Yoo, S. Chen, Y. Li, M. Ge, L. M. Miller, Y. S. Chu *et al.*, "Rapid alignment of nanotomography data using joint iterative reconstruction and reprojection," *Scientific Reports*, vol. 7, 2017.

[31] S. J. Latham, A. M. Kingston, B. Recur, G. R. Myers, O. Delgado-Friedrichs, and A. P. Sheppard, "Reprojection alignment for trajectory perturbation estimation in microtomography," *IEEE Transactions on Computational Imaging*, vol. 4, no. 2, pp. 271–283, 2018. [Online]. Available: https://doi.org/10.1109/TCI.2018.2811945

[32] F. Bleichrodt and K. J. Batenburg, "Automatic optimization of alignment parameters for tomography datasets," in *Scandinavian Conference on Image Analysis*, J.-K. Kamarainen and M. Koskela, Eds., 2013, pp. 489–500.

[33] T. van Leeuwen, S. Maretzke, and K. J. Batenburg, "Automatic alignment for three-dimensional tomographic reconstruction," *Inverse Problems*, vol. 34, no. 2, p. 024004, 2018. [Online]. Available: http://stacks.iop.org/0266-5611/34/i=2/a=024004

[34] S. J. Latham, A. M. Kingston, B. Recur, G. R. Myers, and A. P. Sheppard, "Multi-resolution radiograph alignment for motion correction in X-ray micro-tomography," in *Optics and Photonics: Developments in X-Ray Tomography X*, ser. Proc. SPIE, S. R. Stock, Ed. International Society for Optics and Photonics, 2016, pp. 996 710–996 710.

[35] G. R. Myers, A. M. Kingston, S. J. Latham, B. Recur, T. Li, M. L. Turner, L. Beeching, and A. P. Sheppard, "Rapidly-converging multigrid reconstruction of cone-beam tomographic data," in *SPIE Optical Engineering+ Applications*. International Society for Optics and Photonics, 2016, pp. 99 671M–99 671M.

[36] M. J. Powell, "An efficient method for finding the minimum of a function of several variables without calculating derivatives," *The computer journal*, vol. 7, no. 2, pp. 155–162, 1964.